GiG Research Institute

JOURNAL OF SUSTAINABLE MINING

Volume 21 | Issue 3 Article 5

2022

Effect of mining and geology on mining-induced seismicity – A case study

Author(s) ORCID Identifier:
Heba Khalil: 0000-0002-2862-2560
Tuo Chen: 0000-0002-6551-4091
Yu-Hang Xu: 0000-0002-6222-2296
Hani Mitri: 0000-0002-6482-7424

Recommended Citation

Khalil, Heba; Chen, Tuo; Xu, Yu-Hang; and Mitri, Hani (2022) "Effect of mining and geology on mining-induced seismicity – A case study," *Journal of Sustainable Mining*: Vol. 21 : Iss. 3 , Article 5.
Available at: https://doi.org/10.46873/2300-3960.1361

Effect of mining and geology on mining-induced seismicity – A case study

Abstract

Mining-induced seismicity is a commonly occurring phenomenon in underground mines. This poses a greater challenge to the safety of the mining operation. This paper presents a case study of the Young-Davidson mine in northern Ontario, Canada, where seismic events of magnitude Mn 2.0+ have been observed at mining depths of 600 to 800 m below the surface. The occurrence of large seismic events at such shallow depths is the key issue of this study. A comprehensive study of the microseismic database has been conducted to discern the root causes for the unusually strong seismic activities recorded at shallow depths. The effects of mining activities in the vicinity of two dykes intersecting the orebody on the seismic response are investigated. Variation of the b-value derived from the magnitude-frequency distribution is examined, and moment tensor inversion for three large seismic events is carried out to determine the source mechanisms. It is shown from this investigation that the influence of the sill pillar is more critical, leading to high mining-induced stress and the occurrence of large events. While the findings from this research are specific to this case study, they could be used to shed light on the causes of induced seismicity at other mines with similar conditions.

Keywords

underground mining, mining-induced seismicity, moment tensor inversion, magnitude-frequency distribution

RESEARCH ARTICLE

Effect of Mining and Geology on Mining-Induced Seismicity – A Case Study

Heba I. Khalil [a,*], Tuo Chen [a], Yu-Hang Xu [b], Hani S. Mitri [a]

[a] McGill University, Department of Mining and Materials Engineering, Canada
[b] Alamos Gold Inc., Ontario, Canada

Abstract

Mining-induced seismicity is a commonly occurring phenomenon in underground mines. This poses a greater challenge to the safety of the mining operation. This paper presents a case study of the Young-Davidson mine in northern Ontario, Canada, where seismic events of magnitude Mn 2.0+ have been observed at mining depths of 600–800 m below the surface. The occurrence of large seismic events at such shallow depths is the key issue of this study. A comprehensive study of the microseismic database has been conducted to discern the root causes for the unusually strong seismic activities recorded at shallow depths. The effects of mining activities in the vicinity of two dykes intersecting the orebody on the seismic response are investigated. Variation of the *b*-value derived from the magnitude-frequency distribution is examined, and moment tensor inversion for three large seismic events is carried out to determine the source mechanisms. It is shown from this investigation that the influence of the sill pillar is more critical, leading to high mining-induced stress and the occurrence of large events. While the findings from this research are specific to this case study, they could be used to shed light on the causes of induced seismicity at other mines with similar conditions.

Keywords: underground mining, mining-induced seismicity, moment tensor inversion, magnitude-frequency distribution

1. Introduction

Fracture initiation, propagation, and rock mass movement along pre-existing fracture planes can occur when large volumes of rock are excavated. This process is usually accompanied by the generation of seismic waves known as mining-induced seismicity. As the orebody extends deeper and geologically complex structures are encountered, mining-induced seismic hazards are likely to become more prevalent. Induced seismicity has been recorded in underground mining and civil tunnelling projects worldwide for a wide variety of rock mass environments [1–4]. Mining-induced seismic events take place due to the interaction of tectonic and mining-induced stresses. Seismic events correspond to the sudden release of elastic strain energy in the rock mass and can be represented by the movements caused by the sudden failure of rock masses due to stress concentration in the mining area [3,5]. Mine development activity and ore extraction in underground mines create a high-stress environment that may lead to drastic rock failure, generally known as rockburst. This could result in production losses, equipment damage, and even fatalities because of sudden rock mass failure in mine workings. According to Blake and Hedley [6], a 3.0 magnitude seismic event could cause significant damage to the rockmass, as well as the instability of underground openings, such as triggering rock falls within a 100-m radius of the seismic source. Strong and shallow seismic events can result in the collapse of a mine roof, and for miners working in the vicinity of the falling rock, this poses a direct threat to their lives [2,7]. To mitigate the risks associated with mining-induced seismicity and improve mine safety, many studies focused on forecasting mining-induced seismicity by analysing the microseismic data from microseismic monitoring systems [7–10]. Other

Received 1 April 2022; revised 6 June 2022; accepted 7 June 2022.
Available online 7 November 2022

* Corresponding author.
E-mail address: heba.khalil@mail.mcgill.ca (H.I. Khalil).

https://doi.org/10.46873/2300-3960.1361

researchers attempted to understand rockburst mechanisms to predict seismic hazard through numerical modelling methods [11,12]. This paper presents a case study of the Young-Davidson (YD) mine of Alamos Gold Inc. in northern Ontario, a gold mining operation using a sublevel stoping method with delayed paste fill. The average production of the mine is 8,000 tpd. While deep excavations are normally expected to be associated with strong seismic activities, seismic events of magnitude Mn 2.0+ have been observed at mining depths of only 600–800 m below the surface. The occurrence of large seismic events at such shallow depths is the main concern of this investigation. Thus, the aim of this study is to analyse the microseismic database to understand the mechanisms for the unusually strong seismic activities. Seismicity in mines could be affected by depth, production rate, mine geometry, geological structures such as dykes, faults, or any other geological features, as well as the ambient tectonic stress. In any given case, one or a combination of these factors may play a significant role in induced seismicity [13–15]. Tracking and analysing the causes of mining-induced seismic events would help better understand the influence of such parameters. It could also prove useful for both short and long term mine planning to control the occurrence of strong seismic events and provide a safer work environment throughout the life of a mine plan [16]. The effects of mining parameters and geological conditions on the seismic response in the YD mine are considered in this study. Statistical methods are utilized to characterize the seismic data and predict the trend of seismic hazards. The relation between blasting volume and induced seismicity is analysed, and frequency-magnitude distribution is used for seismicity analysis. The influence of two regional dykes intersecting with the orebody is also examined to reveal the effect of the geological parameters. Furthermore, possible effects of the sill pillar and resulting higher stress regime are explored.

2. Microseismic analysis in underground mines

2.1. Frequency-magnitude distribution

Significant efforts have been made in developing methods to analyse microseismicity in underground mines. One of the most common manipulations of seismic source parameters to obtain more information about the seismic source and describe the event is the frequency-magnitude analysis. Gutenberg and Richter [17] proposed a power law between the event frequency and magnitude.

$$\log N(M) = a - bM \tag{1}$$

In the above $N(M)$ is the total number of microseismic events above magnitude M, and a and b are constants. Fig. 1 shows a graphical representation of two different frequency-magnitude relations for two different datasets. The events are plotted with the magnitude on the x-axis and $N(M)$ on the y-axis. From this distribution, the b-value is an indicator of the seismic hazard as it describes the frequency of occurrence of large events versus small events in a certain area [18]. When the b-value is high (Fig. 1b), the number of large magnitude events is less. If the b-value is low (Fig. 1a), the number of large events is increased, and the stability of rock mass is deteriorated [19]. The b-value can be used to differentiate between the high and low-stressed areas as it is also related to the strength and stress of the medium [20]. In addition, the b-value differs from the seismic mechanism. If seismicity is caused by fault slip, the b-value is usually low (often less than 0.8), whereas when seismicity is due to blasting, the b-values are usually in the range of 1.2–1.5 [21,22]. Thus, the seismic source for the dataset in Fig. 1a is interpreted as fault-slip since a low b-value of 0.5 is obtained. Both datasets in Fig. 1 have nearly the same number of events with a magnitude equaling zero, however, the low b-value for the dataset in Fig. 1a reflects the high proportion of large events, while the group in Fig. 1b has almost no large events but many small events (represented by the high b-value). Thus, comparing the two cases, the seismic hazard is much higher for the group in Fig. 1a [18].

2.2. Moment tensor decomposition and solution

Understanding rock fracturing and failure mode for hazard evolution in underground mines necessitates research into focal mechanisms of induced seismicity. A focal mechanism solution is derived from analysing the waveforms generated by seismic activity and used to illustrate the mechanism of rock failure [23]. The orientation of rock fracturing and type of rupture are quantitatively determined from the moment tensor inversion method using full waveforms and decomposition of the full moment tensor [24]. The moment tensor M represents the source of a seismic event as it describes the deformation at the source location that generates seismic waves based on generalised force couples, arranged in a 3×3 symmetric matrix with six independent

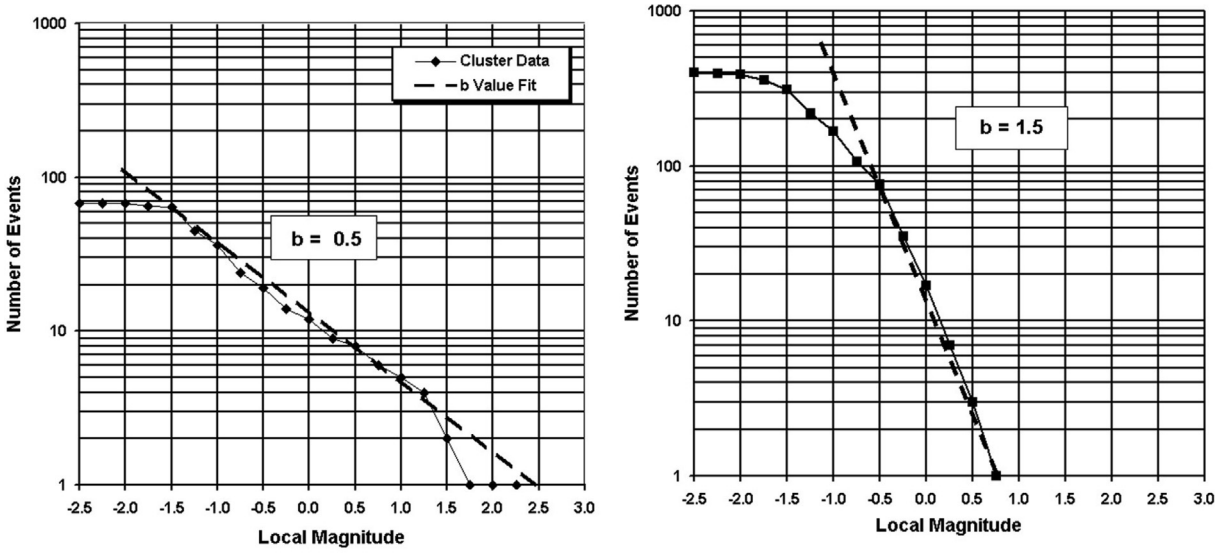

(a) *Low-b value event.* **(b)** *High-b value event.*

Fig. 1. Frequency-magnitude charts for two different groups of events [18].

elements. The moment tensor description is not restricted only to earthquake sources but can also represent other types of seismic sources such as explosions, implosions, and rock falls. The diagonal elements in the moment tensor are called linear vector dipoles. The off-diagonal elements are moments defined by force couples that are equal and opposite in direction [25,26].

$$M = \begin{bmatrix} m_{11} & m_{12} & m_{13} \\ m_{21} & m_{22} & m_{23} \\ m_{31} & m_{32} & m_{33} \end{bmatrix} \quad (2)$$

Beach balls are the graphical representation of the moment tensor. Focal mechanism solution (FMS) beachball diagrams are stereographic projections that depict two black quadrants and two white quadrants divided by two great-circle arcs orientated 90° apart, as shown in Fig. 2a. The potential nodal planes are the great-circle arcs as one of them is parallel to the fault surface that caused the event. Fig. 2b shows the direction of the first motion at the instant of the event, where the motion of the *P*-wave in the medium around the source made the particles in the black quadrants move away from the source whilst the particles in the white quadrants move toward the source. This results from either right-lateral slip in the east-west direction or left-lateral slip in north-south direction.

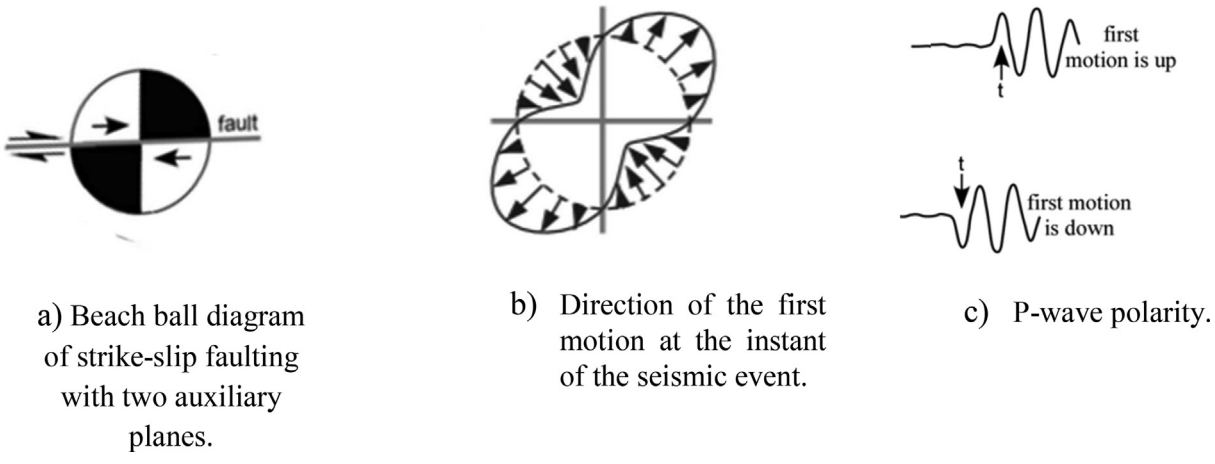

a) Beach ball diagram of strike-slip faulting with two auxiliary planes.

b) Direction of the first motion at the instant of the seismic event.

c) P-wave polarity.

Fig. 2. First motion analysis (after [23]).

Along the fault surface, the slip direction will be from the white to the black quadrant (black arrows). Fig. 2c represents *P*-wave polarity. If the first motion of the *P*-wave is upward on a seismograph, the motion is away from the source and vice versa [23].

The double-couple (DC) source, which reflects the force equivalent of shear faulting, is the most common type of moment tensor. However, some studies show that seismic sources often display more general moment tensors with significant non-double-couple components [27]. An explosion, pillar burst or collapse of a cavity in mines are good examples of a non-DC source [28]. To identify which type of seismic source is represented by the moment tensor, Knopoff and Randall [29] decomposed the moment tensors into three elementary parts; the isotropic (ISO), DC, and compensated linear vector dipole (CLVD) components (Eq. (3)). There are many other decompositions that have been proposed, but Knopoff and Randall decomposition proved to be useful for physical interpretations and became widely accepted [30]. To decompose the moment tensor, the matrix (Eq. (2)) should be rotated to zero the off-diagonal elements. The rotation process creates three orthogonal vectors known as linear vector dipoles. Thus, every moment tensor can be written as three orthogonal linear vector dipoles rotated to a specific orientation (M_1, M_2, and M_3) [31].

$$M = M_{ISO}E_{ISO} + M_{DC}E_{DC} + M_{CLVD}E_{CLVD} \tag{3}$$

where E_{ISO}, E_{DC}, and E_{CLVD} are the ISO, DC, and CLVD elementary tensors, and M_{ISO}, M_{DC} , and M_{CLVD} are the ISO, DC, and CLVD components in the 3-D source-type space.

$$E_{ISO} = \begin{bmatrix} 1 & 0 & 0 \\ 0 & 1 & 0 \\ 0 & 0 & 1 \end{bmatrix}, E_{DC} = \begin{bmatrix} 1 & 0 & 0 \\ 0 & 0 & 0 \\ 0 & 0 & -1 \end{bmatrix}, E^{+}_{CLVD} = \frac{1}{2}\begin{bmatrix} 2 & 0 & 0 \\ 0 & -1 & 0 \\ 0 & 0 & -1 \end{bmatrix}, E^{-}_{CLVD} = \frac{1}{2}\begin{bmatrix} 1 & 0 & 0 \\ 0 & 1 & 0 \\ 0 & 0 & -2 \end{bmatrix} \tag{4}$$

E_{CLVD} is positive when $M_1 + M_3 - 2M_2 \geq 0$ and negative when $M_1 + M_3 - 2M_2 < 0$.

$$M_{ISO} = \frac{1}{3}(M_1 + M_2 + M_3),\ M_{CLVD} = \frac{2}{3}(M_1 + M_3 - 2M_2),\ M_{DC} = \frac{1}{2}(M_1 - M_3 - |M_1 + M_3 - 2M_2|) \tag{5}$$

The isotropic component, M_{ISO} is the portion of the tensor that represents a uniform volume change. A positive M_{ISO} is an expansion or explosion, which may be a confined blast or rock bulking, while a negative M_{ISO} is a contraction or implosion. Implosion may indicate a pillar bursting, buckling, or rock ejecting into a void [24,32]. Isotropic components that are less than 10% of the whole moment tensor are generally deemed insignificant. The deviatoric tensor results in displacement with zero net volume change like the geological process of a fault dislocation. The general dislocation can be a mix of shear and normal dislocation [25]. To better understand the relative quantities of shear and normal displacements, the deviatoric component is divided into the DC and CLVD elemental sources, according to Knopoff and Randall [29].

The DC source, M_{DC}, is a pure shear mechanism. It is referred to as a double couple because there are two equal and opposite force couples, and the displacement pattern is the same for both force couples. As a result, there are two possible fault plane orientations that model the expected displacement equally well. Then, a pure DC source has two equal and opposite linear vector dipoles while the third dipole is zero [25,30]. This can be clearly illustrated in the elementary DC tensor in Eq. (4).

The CLVD, M_{CLVD}, source is a normal dislocation on a plane. The normal displacement from one linear vector dipole is compensated by opposing displacement from the other two linear vector dipoles, and thus, there is no net volume change. For a positive CLVD source, a single tensile dipole is compensated by two compressive dipoles and the inverse for a negative CLVD source [33]. That can be clearly portrayed in the elementary CLVD tensor in Eq. (4). A pure CLVD source represents a Poisson's ratio of 0.5 [33], which has no geological meaning. However, it can make sense for a mixed source event, such as an event with partial isotropic and CLVD components [34].

Microseismic events are normally represented by a combination of these three simple mechanisms. Thus, it is very important to decompose a seismic source event into standard forms of ISO, DC, and CLVD components to understand a complex event [35]. The moment tensor decomposition can be interpreted using the Hudson chart, which is a useful plot to display the moment tensor decomposition and to show the position of the source in the CLVD-ISO coordinate system. Fig. 3 shows the Hudson chart, which is generated using mXrap software. It represents the relative proportions of ISO, DC and CLVD elemental sources. The vertical

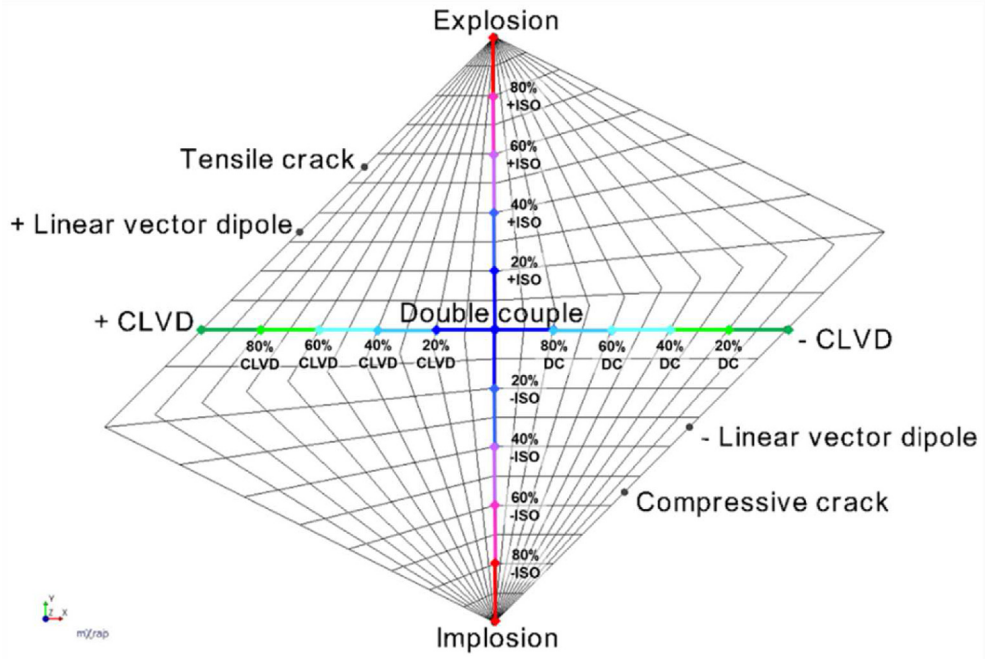

Fig. 3. Hudson chart (after [37]).

axis is the ISO component ranging from −100% (implosion) to +100% (explosion). The horizontal axis shows the CLVD component from +100 to −100%, which represents faulting on non-planar faults, with 100% DC at the centre, which indicates pure shear faulting (0% ISO, 0% CLVD). The outer border of the chart is the 0% DC where pure tensile and compressive cracks are plotted [25,36].

3. Case study – Young-Davidson Mine

3.1. Mine location

Young-Davidson Mine is a gold mining operation located in northern Ontario near Matachewan town (Canada), as shown in Fig. 4. The mine is owned and operated by Alamos Gold Inc. The orebody strike runs east-west with mineralization extending to depths of about 1,500 m [38].

3.2. Mine geology

Young-Davidson property exists in the south-western part of the Abitibi Greenstone Belt. The mine lies within the Kirkland Larder Lake gold belt, which includes the world-class Kerr-Addison-Chesterville gold deposits and is intersected by the regional Larder Lake–Cadillac Fault Zone, known for its spatially associated gold camps. The property is hosted in a felsic intrusive syenite unit of about 1,420 m east-west by 470 m north-south. The Timiskaming Sediments are mainly the footwall rock type and are also found to be inter-bedded layers throughout the syenite rock mass. The hanging wall of the deposit is predominantly mafic volcanic, consisting of inter-bedded mafic flows and ultramafic flows. The gold mineralization is mostly related to quartz veins and disseminated pyrite mineralization, hosted in a felsic intrusive syenite unit. Several mineralized gold zones are hosted in the syenite. All lithologies are cut by late, generally northeast-trending Proterozoic diabase dikes, as shown in Fig. 5 [38].

3.3. Site ESG seismicity monitoring system

As of December 2020, the seismic monitoring system used at the YD mine included 46 working sensors providing coverage for the production areas down to the 9305 level in the mine plan (1 km depth). The system includes 34 uniaxial sensors, eight triaxial sensors, three 4.5 Hz Strong Ground Motion (SGM) sensors underground, besides one 2.0 Hz SGM sensor on the surface. Instead of using a constant velocity model, a 3D Velocity Model that considers different lithology groups, paste-filled stopes and mined-out areas has been used and updated semi-annually since 2018. That was very useful to improve source location accuracy. The

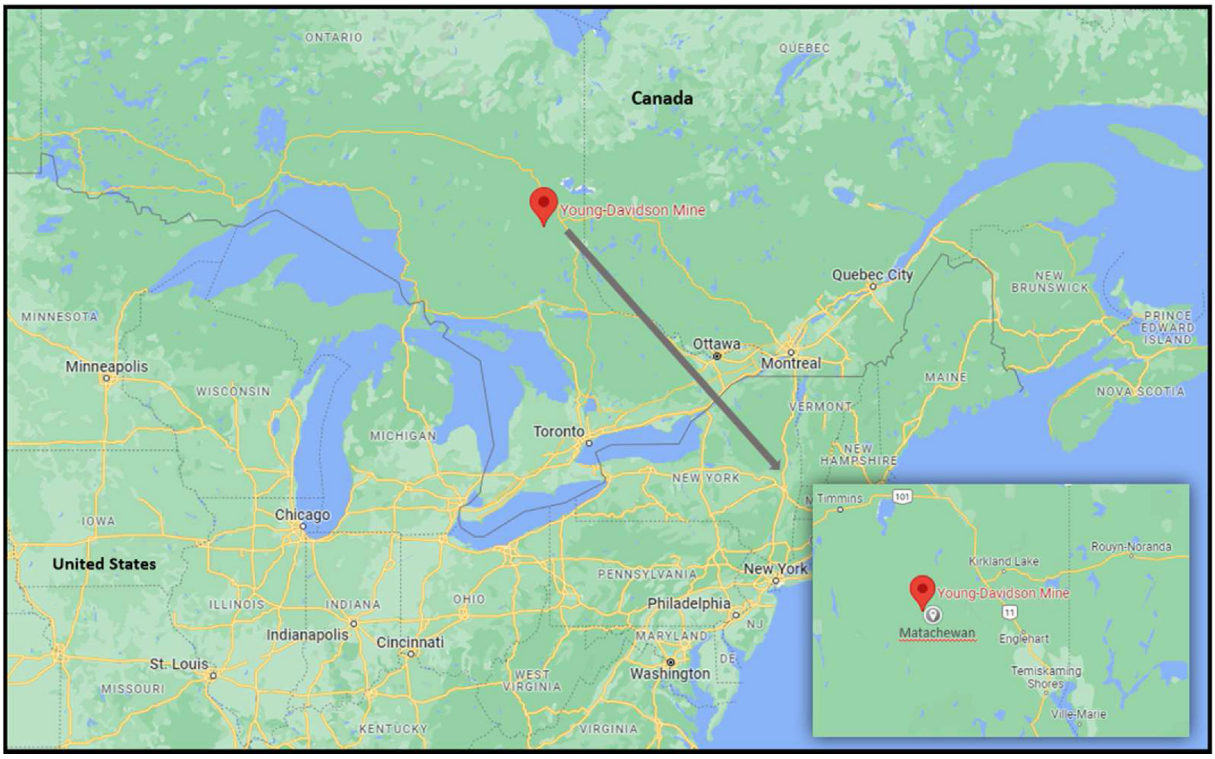

Fig. 4. Location map of Young-Davidson Mine.

mine consists of three main geological domains: host rock (Timiskaming sediments), diabase and syenite (ore), as shown in Fig. 6.

3.4. YD large events

YD large events recorded from August 2018 to March 2021 are reported in Table 1. The large events are recorded by Canadian National Seismograph Network (CNSN) as the sensitivity and accuracy of the CNSN are relatively constant compared with the YD seismic monitoring system. This study will focus on M_N 2+ events YD mine experienced in 2020. As mentioned earlier, most large events occurred at depths of only 600–800 m below the surface. There is no apparent correlation between the increase of mining depth and seismic magnitude, which in turn suggests that those large events are likely driven by other factors like mining activities or geological structures, e.g., dykes intersecting the orebody.

4. Correlation between induced seismicity and mining production rate

To identify the reasons beyond the large seismic events, the effect of the blasting volume on mine seismicity is analysed. Fig. 7a shows the production blasting activity in 2020, where the blasting volume ranges from 40,000 to 200,000 tons per month, and the peak months are January, September, and October. Comparing the accumulated seismic moment represented in Fig. 7b and accumulated seismic energy in Fig. 7c with monthly blasting volume reveals that blasting affects the mine seismicity at some points as in January, October, and December. However, the peak accumulated seismic moment or energy does not always coincide with peak production blasting. In June, the low production rate is associated with a high seismic moment and high seismic energy, whereas in September, the high production rate resulted in relatively low seismic energy. Thus, it can be concluded that there is no apparent correlation between the accumulated seismic moment or energy and the monthly blasting volume in 2020.

5. *b*-value analysis

5.1. Variation in b-value with blasting distance from the dykes

To analyse the effect of the geological structures on seismicity, the variation in the *b*-value is investigated for the mining depth range of 700–900 m (levels 9600 to 9400). Fig. 8 is a plan view showing the NE trending diabase dykes intersecting with the orebody at level 9470. Also, the four largest events that

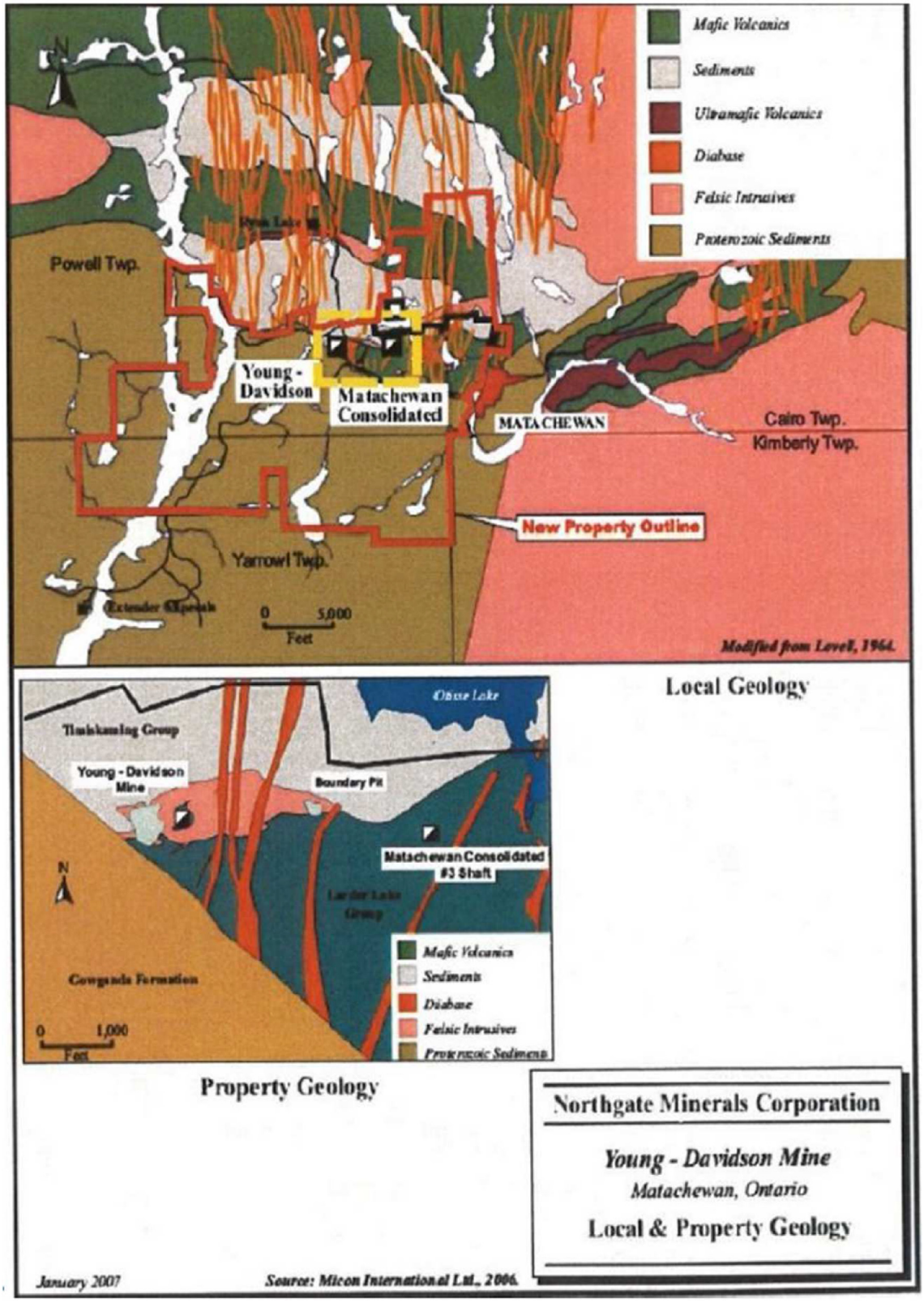

Fig. 5. Local geology of the Young-Davidson Property [38].

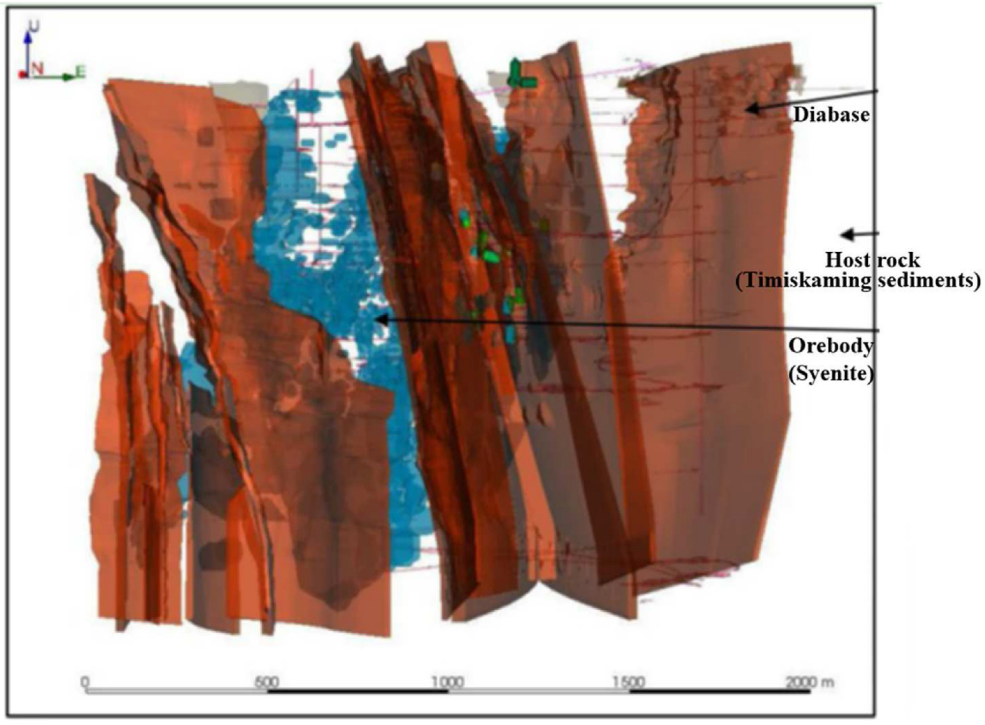

Fig. 6. Three main geological domains in YD mine: Timiskaming sediments (host rock), diabase and syenite (ore) [39].

occurred around this depth level in 2020 are marked as yellow circles in Fig. 8. The change in the *b*-value with the distance of the blasting from the dykes has been analysed in three different zones separated by two major dykes (dyke A and dyke B). The analysis is conducted separately in each zone as the stress conditions may be different. The *b*-values of blasting-induced seismicity west of dyke A are plotted in Fig. 9a, whereas the *b*-values east of dyke B are shown in Fig. 9b. The *b*-values recorded between dyke A and dyke B are plotted in Fig. 9c. The dot colour on the charts indicates the blasting volume.

Table 1. YD large events recorded by CNSN (2018.05–2021.03) [39].

EST Time		Depth (km)	Nuttli Magnitude, M_N
2018/08/12	19:40:34	0.8	1.6
2018/08/24	3:33:19	0.8	1.9
2018/09/10	16:44:54	0.5	2.2
2018/09/12	7:58:42	0.6	3.0
2018/09/12	10:02:07	0.6	2.2
2018/10/27	5:59:34	0.6	1.7
2018/11/12	12:01:50	0.5	1.9
2019/05/17	2:13:14	1.0	1.6
2019/09/19	4:53:20	0.7	2.6
2019/09/21	4:45:43	0.6	2.3
2020/02/20	7:09:32	0.3	2.2
2020/06/23	13:05:48	0.8	2.4
2020/10/21	16:31:29	0.8	1.7
2020/10/21	16:52:07	0.8	2.4
2020/10/30	12:44:04	0.8	2.2
2020/11/30	1:12:11	0.9	2.0
2020/12/02	17:38:26	0.6	2.4
2020/12/09	13:03:12	0.8	2.3
2020/12/18	5:37:02	0.7	2.0
2021/01/09	5:36:19	0.8	2.7
2021/01/19	6:03:04	0.8	2.5
2021/02/25	17:41:34	0.7	2.9
2021/03/03	4:11:08	0.9	2.3

5.2. Discussion of b-value results

From Fig. 9a, *b*-values close to dyke A are relatively high, with values greater than 1. This suggests that dyke A may not be the main contributor to the two large events (1) and (2) that occurred on October 30 and December 09 west of dyke A. Fig. 9b shows that *b*-values are smaller east of dyke B, being lower than 1. This implies high-stress condition and explains the occurrence of the two large events (3) and (4) on June 23 and October 21, respectively. Event (4) can be attributed to a large blast 10 m east dyke *B* with a corresponding *b*-value of 0.47. This is followed by another bigger blast on the same day 60 m east of dyke B that resulted in a significantly higher *b*-value. Such high *b*-value may be explained by the stress relief due to rock-mass damage that took place earlier after the first blast and triggered the large event (4). The low *b*-

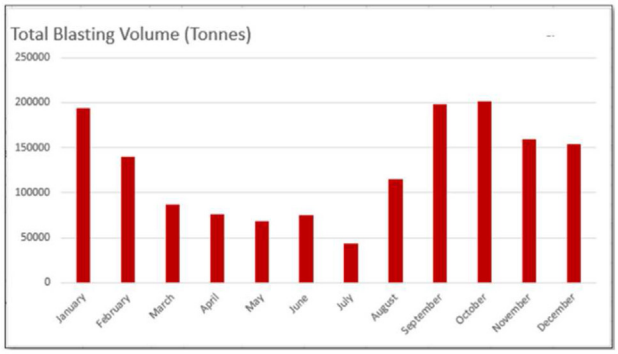

(a) *Total blasting volume.*

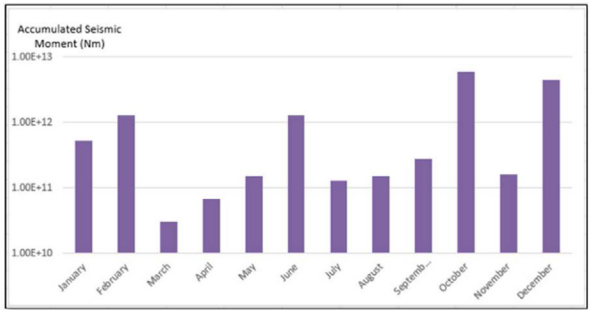

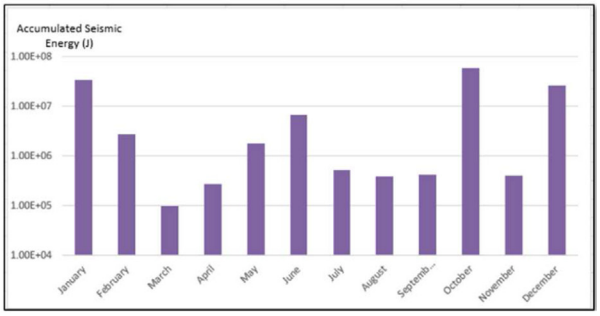

(b) *Accumulated seismic moment.* (c) *Accumulated seismic energy.*

Fig. 7. Relation between mining production rate and recorded seismicity throughout 2020.

values 60 m east dyke B may be due to stoping activities causing local stress concentrations around the blasted areas after the December 22 and 26 blasts. Examining the influence of stope sequencing should provide more insight into the causative factors, however, it is not in the scope of the current work. Fig. 9c shows that the zone between the two dykes is relatively stressed based on the low b-values obtained. It is noteworthy that the available database is not large enough to show definite trends

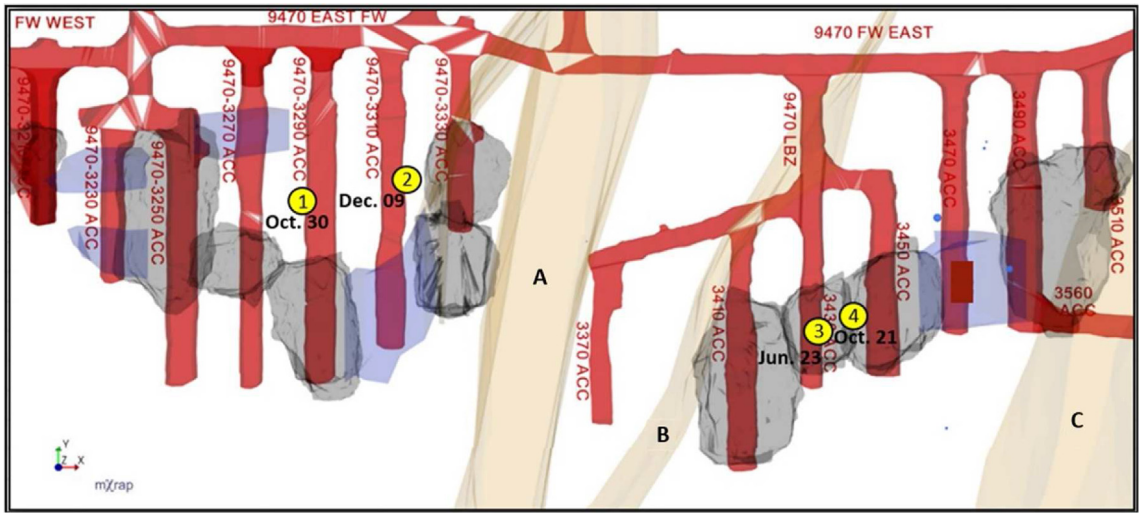

Fig. 8. Plan view of level 9470 showing four largest events in 2020 between levels 9400 and 9600.

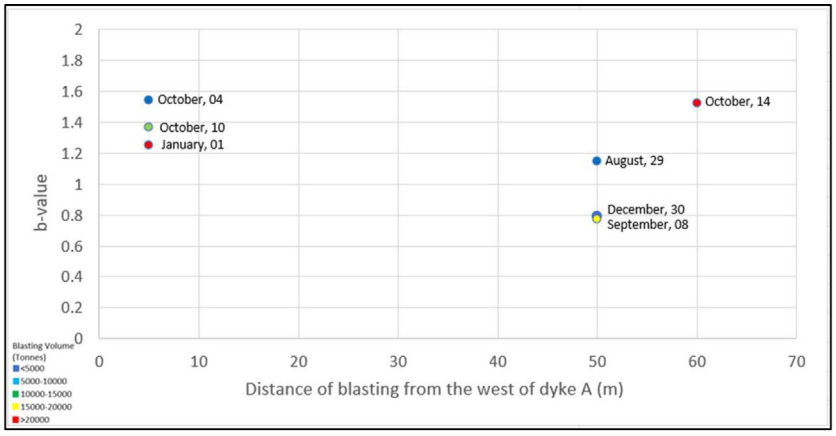

(a) *West of dyke A.*

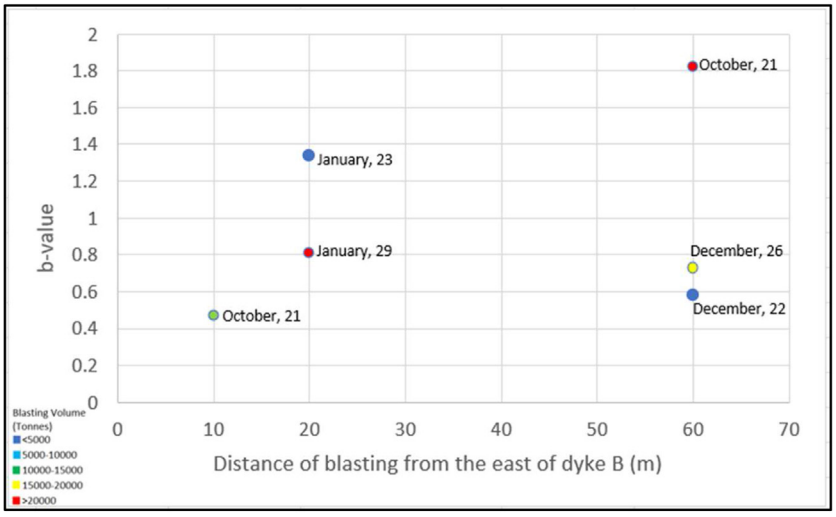

(b) *East of dyke B.*

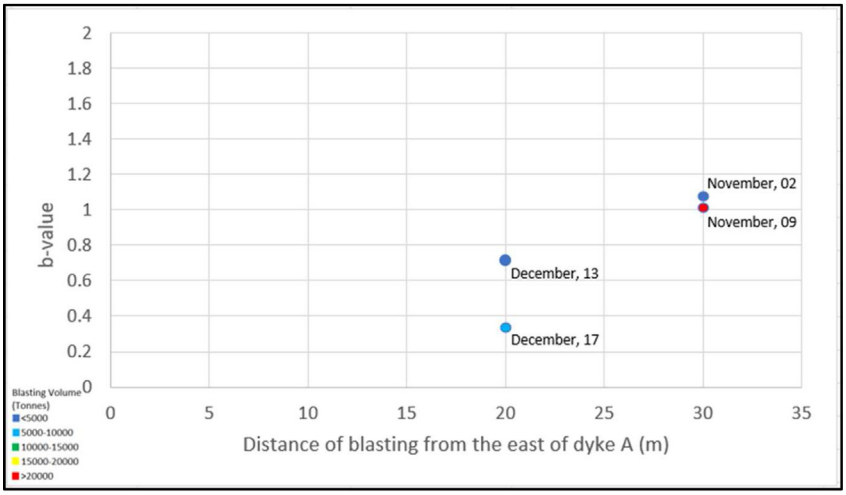

(c) *Between dyke A and dyke B.*

Fig. 9. b-value results.

Table 2. Moment tensor decompositions and source mechanisms reported for the three events.

Event	Event no.	ISO%	CLVD%	DC%	M_w	Failure mechanism
Oct. 30	1	−19.0807	−42.2411	38.6782	2.4676	Compressional failure
Dec. 09	2	−19.9872	−42.9797	37.0331	2.4845	Compressional failure
Oct. 21	4	−23.9782	−53.5614	22.4604	2.0013	Compressional failure

based on *b*-values. Better representation of *b*-values would be achieved using more data from 2021 in the next step of this project.

6. Moment tensor inversion

6.1. Moment tensor inversion method

For the analysis of large events, moment tensor inversion is conducted using HybridMT software package developed in MATLAB for three events [40]. Full seismograms measured by the seismic acquisition system as well as accurate synthetic seismograms of the Earth (Green's function G) are required for moment tensor inversion. Green's function computes the ground displacement recorded by the seismic sensor and describes all wave propagation effects, including the elastostatic response of the Earth. The ground motion response $u(t)$ at a station depends on $G(t)$. Thus, the moment tensor inversion is based on Eq. (6). When inverting this expression, the least-square method is often used for calculating the moment tensor as represented in Eq. (7) [41].

$$u = GM \tag{6}$$

where M represents moment vector (6×1) composed of six independent components of the moment tensor, u is the $(n \times 1)$ vector representing observed amplitudes at sensors where n is the number of observed amplitudes for a given event, and G is the $(n \times 6)$ Green's function derivatives matrix, which represents the response of the medium from the source to the sensor. Eq. (6) can be rearranged as follows.

$$M = \left(G^T G\right)^{-1} G^T u \tag{7}$$

The moment tensor inversion software Hybrid MT performs moment tensor inversion for earthquake data recorded by regional-to-local seismic networks. The algorithm inverts for unconstrained full, deviatoric, and double-couple constrained moment tensors using first *P*-wave amplitudes. The amplitudes, rupture time, and polarity of the *P*-wave first motions are required as input data for the MT inversion. In addition, the location of the seismic network, as well as the velocity model, must be specified. The seismic parameters and graphical representations of the moment tensor are then calculated in the MATLAB environment [40].

6.2. Moment tensor inversion results

FMS results of each event decompose the seismic MT into its ISO and Deviatoric parts, including the CLVD and the DC components, following the decomposition introduced by Knopoff and Randall [29]. Also, the solution specifies the seismic moment and moment magnitude as well as the potential nodal planes of each event. The MT graphical representation (beach balls) is also generated, showing the best double-couple nodal lines, station locations on the focal sphere, and the location of pressure (*P*) and tension (*T*) axes [40].

The moment tensor decompositions in Table 2 show that the percentage of the DC component for the three events is less than 50%, indicating that shear failure is not dominant in these events. On the other hand, the negative ISO components imply that the sources have encountered implosive deformation, a characteristic feature of compressional failure. As these events also show negative CLVD components, it is possible to infer that they are relevant to collapse. Table 2 shows that the source mechanisms are very close for the three events, and it is the most properly compressional failure, especially for events (1) and (2) where the deviatoric percentages are almost the same. Table 3 lists the resolved fault plane solutions derived from the DC component of the full moment tensor for the three events. Event (4) suggests a strike-slip fault that has nodal planes striking NNE-SSW and NNW-SSE,

Table 3. Fault plane solutions for the three events and corresponding fault types.

Event	Event no.	Strike1	Dip1	Rake1	Strike2	Dip2	Rake2	Fault type
Oct. 30	1	100.19	67.21	131.84	213.58	46.62	32.20	Oblique-thrust fault
Dec. 09	2	100.92	63.89	129.39	219.11	46.06	37.68	Oblique-thrust fault
Oct. 21	4	134.66	83.78	−151.33	41.27	61.52	−7.08	Strike-slip fault

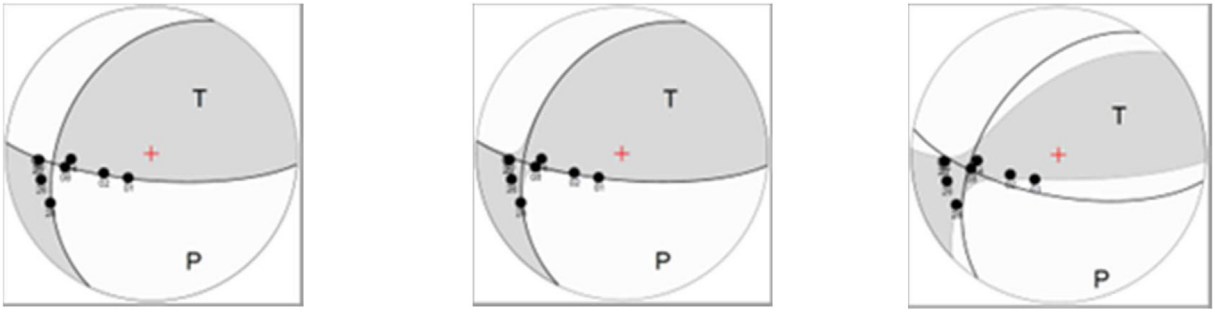

(a) DC component. (b) Deviatoric component. (c) Full tensor.

Fig. 10. Generated beachballs from focal mechanism solution of the event (1).

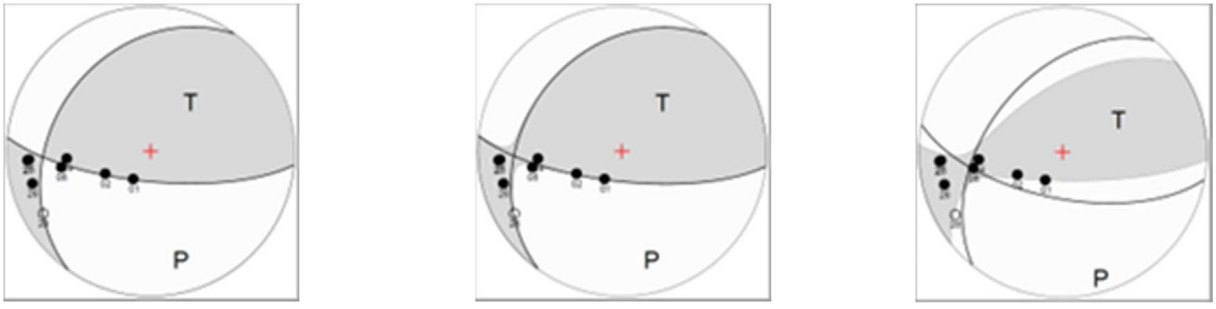

(a) DC component. (b) Deviatoric component. (c) Full tensor.

Fig. 11. Generated beachballs from the focal mechanism solution of the event (2).

while events (1) and (2) suggest an oblique-thrust fault that has a reverse component of slip. Fig. 10, 11, and 12 present the generated beachballs of the full, deviatoric, and double couple components for the events (1), (2), and (4), respectively.

To further identify the source mechanisms of these events, the three seismic events are plotted on the Hudson source-type diagram, as shown in Fig. 13. The events are clustered at the right-bottom quadrant of the Hudson diagram, and the locations indicate a compressional failure mechanism with a small part of shear.

It is essential to point out that MT inversion is sensitive to the quality of the input data, sensor

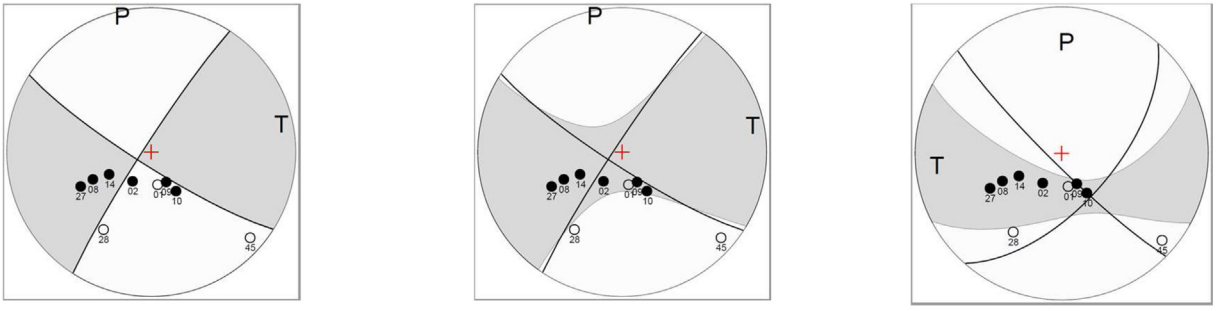

(a) DC component. (b) Deviatoric component. (c) Full tensor.

Fig. 12. Generated beachballs from focal mechanism solution of the event (4).

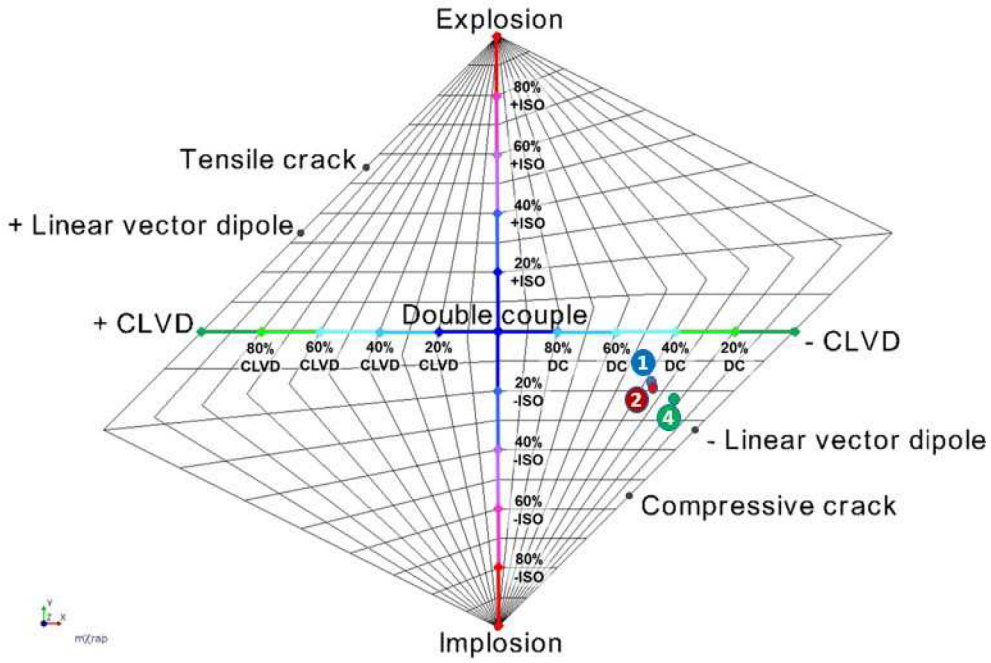

Fig. 13. Hudson source-type plot of the three events 1, 2, and 4.

coverage and modelling assumptions. This includes polarity and amplitude reading biases for waveform data with low signal-to-noise ratios, synthetic waveform mismodeling due to a lack of insight into the medium (velocity model, rock anisotropy), and eventually site effects and sensor features (coupling, limited frequency band, polarity) [42]. Focal mechanism solutions help us better understand the root causes behind the large event, however, sensor coverage for the solved events cannot be considered ideal, as represented by the generated beachballs.

7. Effect of stoping sequence on the studied seismicity

To reveal the relation between induced seismic events and mining structure, the event locations and time with respect to stope sequencing have been

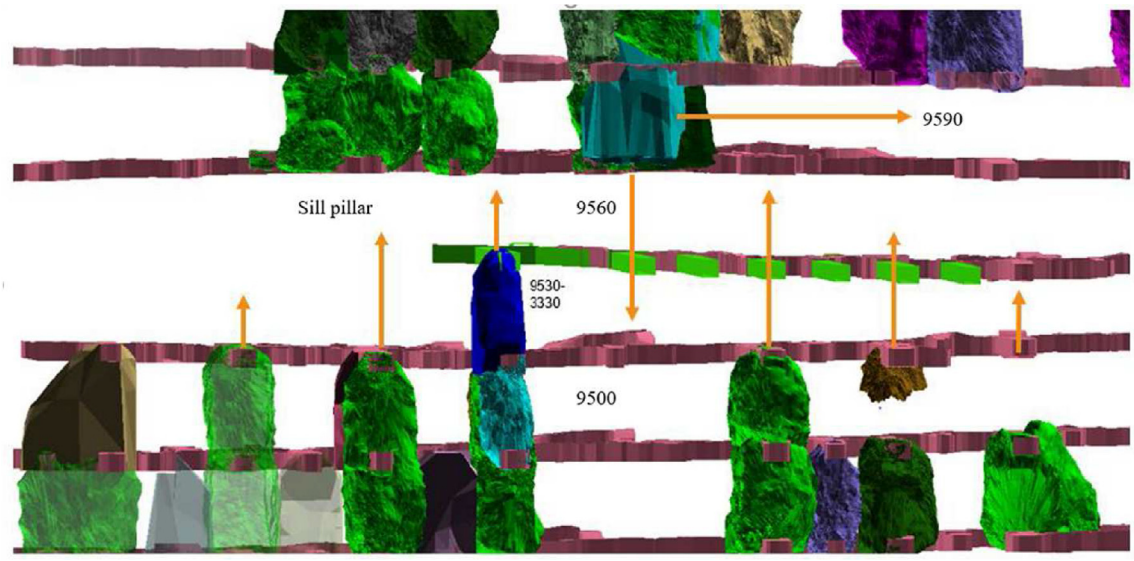

Fig. 14. Planned stoping progression for the 9590 breakthrough [43].

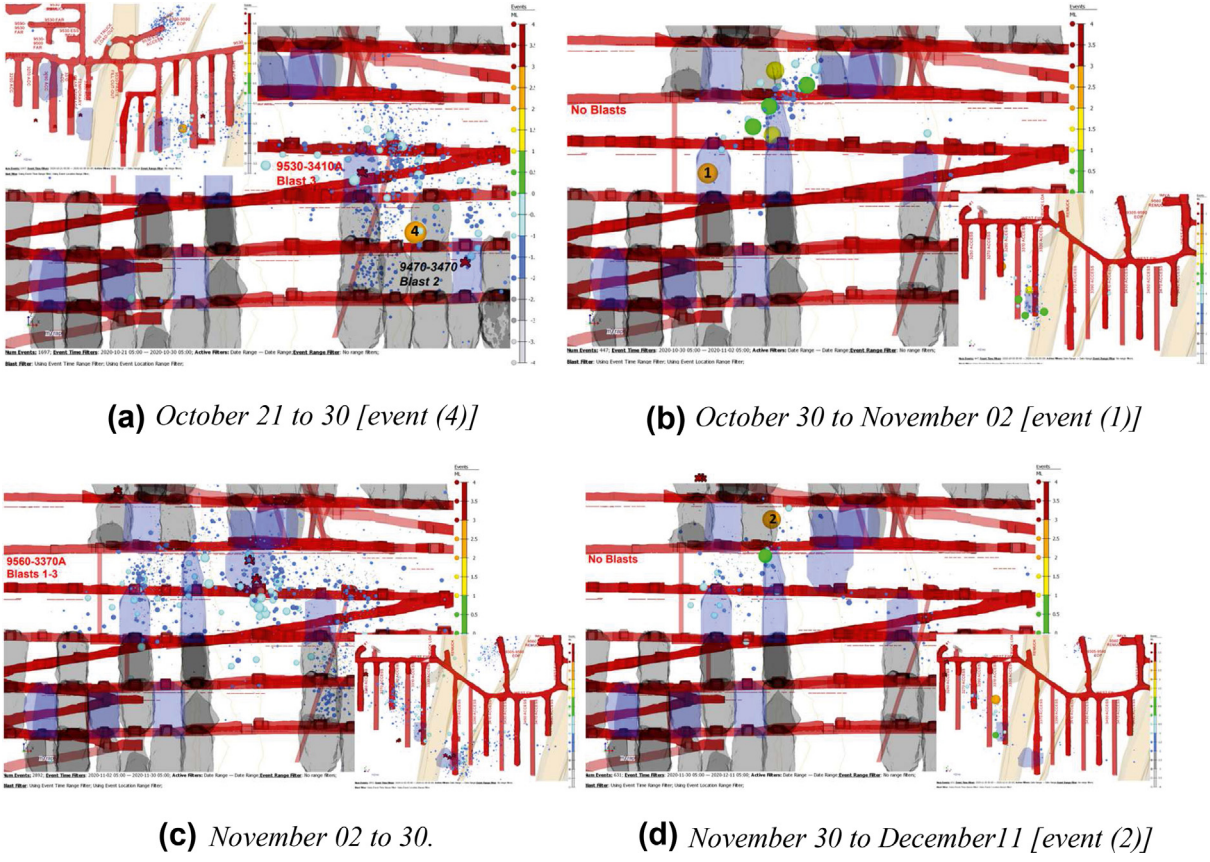

(a) *October 21 to 30 [event (4)]*

(b) *October 30 to November 02 [event (1)]*

(c) *November 02 to 30.*

(d) *November 30 to December11 [event (2)]*

Fig. 15. Mining sequence and large seismic events through levels 9400 to 9600 between October and December 2020. Note: Orange circles represent large events.

analysed. Stope sequencing is bottom-up for each mining zone, and the plan calls for a 30 m sill pillar between mining zones. Late development on level 9560 (740 m below surface) due to low-grade material created a long sill pillar. Sill pillar recovery was implemented between levels 9590 and 9560. An increase in seismic activities was recorded during pillar recovery. Stoping breakthrough occurred at the 3330-easting, where stress can be re-distributed to the 3370-easting and outer abutments. The 9590 stoping progress is eastward. Fig. 14 shows the planned stoping progression for the 9590 breakthrough [43].

Efforts were made to optimize stope sequencing to reduce significant stress redistribution after pillar yielding. However, the sequence was still accompanied by high seismic activities. Fig. 15 shows four cross sections illustrating the stoping sequence in the studied level (9400–9600) toward the sill pillar, triggering large events (orange balls). Fig. 15a depicts blasting in the period from October 21 to 30; it shows the location of the event (4). Fig. 15b indicates that there was no blast from October 30 to November 02, yet it shows the occurrence of event (1). Fig. 15c covers the sequence from November 02 to November 30. The last cross section (d) illustrates that there was no blast from November 30 until December 11 at this depth level, but a large event (2) occurred on December 09. It is worth noting that the analysed large events (1) and (2) happened while mining toward the sill pillar, which would explain the similar focal mechanism solutions for both events.

8. Conclusions

In this paper, a preliminary study of the microseismicity at the YD mine has been conducted to understand the root causes of the unusually strong seismic events recorded at shallow depths. The impact of blasting volume on accumulated seismic moment and energy was first investigated. It is found that there is no apparent correlation between blasting volume and accumulated seismic moment or energy in the studied area. In addition, the stress regime of mining zones that intersected with

regional dykes is studied by the *b*-value analysis through the mining levels 9400 to 9600. As for the zone east of dyke B, where two events (3) and (4) occurred, the analysis shows low *b*-values reflecting a highly stressed zone. Event (4) is likely triggered by large volume blasting, but more investigation is required to understand event (3) better. The *b*-values west of dyke A are quite high, indicating that the dyke is not the primary cause of the two major events (1) and (2). For further analysis, the moment tensor inversion was performed for three major events using HybridMT MATLAB code to reveal the event focal mechanisms. Focal mechanism solutions for three events, namely (1), (2), and (4), show almost the same failure mechanism, which is compressional failure. The percentage of DC components for the three events is less than 50%, indicating that shear failure is not prevalent in these events, whereas the negative ISO components indicate that the sources experienced implosive deformation, which is a characteristic feature of compressional failure. It is possible to infer that these events are relevant to collapse because they also show negative CLVD contributions. The possible mechanisms for the three events are further confirmed based on mining sequences. Events (1) and (2) occurred while mining toward the sill pillar, which demonstrates the consistency in their focal mechanism solutions. Thus, sill pillar recovery might be the main contributor to increased mining-induced seismicity. Studying the FMS for more events in future can provide additional information about the slip plane and help predict the trend of seismic hazards, which will be very useful in future mine planning and mine safety. While the findings from this research are specific to the case study of the YD Mine, they could be used to shed light on the causes of induced seismicity at other mines with similar conditions.

Ethical statement

The authors state that the research was conducted according to ethical standards.

Funding body

This research was funded by Natural Sciences and Research Engineering Council of Canada (NSERC), fund number *223079*.

Conflict of interest

The authors declare no conflict of interest.

Acknowledgments

This work is financially supported by Natural Sciences and Research Engineering Council of Canada (NSERC) - Discovery Program Grant by Natural Sciences and Research Council of Canada. The authors wish to thank Alamos Gold Inc. for the co-operation and the support with the data of Young-Davidson Mine for this study.

References

[1] Li T, Cai MF, Cai M. A review of mining-induced seismicity in China. Int J Rock Mech Min Sci 2007 Dec 1;44(8):1149–71. https://doi.org/10.1016/j.ijrmms.2007.06.002.
[2] He S, Chen T, Vennes I, He X, Song D, Chen J, et al. Dynamic modelling of seismic wave propagation due to a remote seismic source: a case study. Rock Mech Rock Eng 2020 Nov; 53(11):5177–201.
[3] Brown LG, Hudyma MR. Mining induced seismicity in Canada: a 2017 update. In: 52nd US rock mechanics/geomechanics symposium. OnePetro; 2018 Jun 17.
[4] Lovchikov AV. Review of the strongest rockbursts and mining-induced earthquakes in Russia. J Min Sci 2013 Jul; 49(4):572–5.
[5] Zhou XP, Qian QH, Yang HQ. Rock burst of deep circular tunnels surrounded by weakened rock mass with cracks. Theor Appl Fract Mech 2011 Oct 1;56(2):79–88. https://doi.org/10.1016/j.tafmec.2011.10.003.
[6] Blake W, Hedley DG. Rockbursts: case studies from North American hard-rock mines. SME; 2003.
[7] Ilieva M, Rudziński Ł, Pawłuszek-Filipiak K, Lizurek G, Kudłacik I, Tondaś D, et al. Combined study of a significant mine collapse based on seismological and geodetic data—29 January 2019, Rudna Mine, Poland. Rem Sens 2020 Jan; 12(10):1570. https://doi.org/10.3390/rs12101570.
[8] Si G, Cai W, Wang S, Li X. Prediction of relatively high-energy seismic events using spatial–temporal parametrisation of mining-induced seismicity. Rock Mech Rock Eng 2020 Nov;53(11):5111–32.
[9] He S, Song D, Mitri H, He X, Chen J, Li Z, et al. Integrated rockburst early warning model based on fuzzy comprehensive evaluation method. Int J Rock Mech Min Sci 2021 Jun 1; 142:104767.
[10] Lurka A. Spatio-temporal hierarchical cluster analysis of mining-induced seismicity in coal mines using Ward's minimum variance method. J Appl Geophys 2021 Jan 1;184: 104249.
[11] He S, Chen T, Song D, He X, Chen J, Li Z, et al. A new methodology for the simulation of tunnel rockburst due to far-field seismic event. J Appl Geophys 2022 Jul 1;202:104651.
[12] Wang J, Apel DB, Pu Y, Hall R, Wei C, Sepehri M. Numerical modeling for rockbursts: a state-of-the-art review. J Rock Mech Geotech Eng 2021 Apr 1;13(2):457–78.
[13] Gibowicz SJ, Kijko A. An introduction to mining seismology. Int Geophys Ser 1994;55. i–x.
[14] Holub K. Predisposition to induced seismicity in some Czech coal mines. In: Seismicity Associated with Mines, Reservoirs and Fluid Injections. Basel: Birkhäuser; 1997. p. 435–50. https://doi.org/10.1007/s000240050086.
[15] Brown LG. Quantification of seismic responses to mining using novel seismic response parameters (Doctoral dissertation. Laurentian University of Sudbury); 2018.
[16] Leake MR, Conrad WJ, Westman EC, Afrouz SG, Molka RJ. Microseismic monitoring and analysis of induced seismicity source mechanisms in a retreating room and pillar coal mine in the Eastern United States. Undergr Space 2017 Jun 1;2(2): 115–24. https://doi.org/10.1016/j.undsp.2017.05.002.

[17] Gutenberg B, Richter CF. Frequency of earthquakes in California. Bull Seismol Soc Am 1944;34(4):185–8.
[18] Hudyma MR. Analysis and interpretation of clusters of seismic events in mines. University of Western Australia; 2008 Nov.
[19] Yu Q, Zhao D, Xia Y, Jin S, Zheng J, Meng Q, et al. Multivariate early warning method for rockburst monitoring based on microseismic activity characteristics. Front Earth Sci 2022 Jan 25:19. https://doi.org/10.3389/feart.2022.837333.
[20] Xu NW, Dai F, Zhou Z. Study of characteristics of b value for microseismic events in high rock slope. Chin J Rock Mech Eng 2014;33(S1):3368–74.
[21] Legge NB, Spottiswoode SM. Fracturing and microseismicity ahead of a deep gold mine stope in the pre-remnant and remnant stages of mining. In: 6th ISRM Congress. OnePetro; 1987 Aug 30.
[22] Hudyma MR. Seismicity at Brunswick mining. InProceedings quebec mining association ground control colloque. Quebec: Val D'Or; 1995.
[23] Cronin V. A draft primer on focal mechanism solutions for geologists. Texas. Baylor University; 2004. p. 14.
[24] Ma J, Dong L, Zhao G, Li X. Focal mechanism of mining-induced seismicity in fault zones: a case study of yongshaba mine in China. Rock Mech 2019 Sep;52(9):3341–52. https://doi.org/10.1007/s00603-019-01761-4.
[25] Dahm T, Krüger F. Moment tensor inversion and moment tensor interpretation. InNew Manual of Seismological Observatory Practice vol. 2 (NMSOP-2) 2014 (pp. 1-37). Deutsches GeoForschungsZentrum GFZ. DOI:10.2312/GFZ.NMSOP-2_IS_3.9
[26] Eyre ST, Van Der Baan M. Introduction to moment tensor inversion of microseismic events. GeoConvention 2015 May. https://doi.org/10.1190/tle34080882.1.
[27] Julian BR, Miller AD, Foulger GR. Non-double-couple earthquakes 1. Theory. Rev Geophys 1998 Nov;36(4):525–49. https://doi.org/10.1029/98RG00716.
[28] Šílený J, Milev A. Source mechanism of mining induced seismic events—resolution of double couple and non-double couple models. Tectonophysics 2008 Aug 1;456(1–2):3–15. https://doi.org/10.1016/j.tecto.2006.09.021.
[29] Knopoff L, Randall MJ. The compensated linear-vector dipole: a possible mechanism for deep earthquakes. J Geophys Res 1970 Sep 10;75(26):4957–63. https://doi.org/10.1029/JB075i026p04957.
[30] Vavryčuk V. Moment tensor decompositions revisited. J Seismol 2015 Jan;19(1):231–52. https://doi.org/10.1007/s10950-014-9463-y.
[31] Tape W, Tape C. A geometric setting for moment tensors. Geophys J Int 2012 Jul 1;190(1):476–98. https://doi.org/10.1111/j.1365-246X.2012.05491.x.
[32] Malovichko D, van Aswegen G, Clark R. Mechanisms of large seismic events in platinum mines of the Bushveld Complex (South Africa). J S Afr Inst Min Metall 2012 Jun;112(6):419–29.
[33] Lay T, Wallace TC. Modern global seismology. Elsevier; 1995 May 18.
[34] Eaton DW. Microseismic focal mechanisms: a tutorial, vol. 20. Calgary, Alberta: CREWES Research Report; 2008. p. 1. 1.
[35] Krieger L, Heimann S. MoPaD—moment tensor plotting and decomposition: a tool for graphical and numerical analysis of seismic moment tensors. Seismol Res Lett 2012 May 1;83(3):589–95. https://doi.org/10.1785/gssrl.83.3.589.
[36] Tierney S. Moment tensors – a practical guide, blog post, 2019. Perth, Western Australia: Australian Centre for Geomechanics, The University of Western Australia; 2015. Figure generated by Harris, PH & Wesseloo, J, mXrap software, version 5, https://mxrap.com/moment-tensors-a-practical-guide. https://mxrap.com.
[37] Hudson JA, Pearce RG, Rogers RM. Source type plot for inversion of the moment tensor. J Geophys Res Solid Earth 1989 Jan 10;94(B1):765–74. https://doi.org/10.1029/JB094iB01p00765.
[38] Alamos Gold Inc. Mines and projects. Retrieved September 14th, 2015, from Alamos Gold: http://www.alamosgold.com/mines-and-projects/producing-mine/Young-Davidson/.
[39] Alamos Gold Inc. Seismic risk management plan. 2021.
[40] Kwiatek G, Martínez-Garzón P, Bohnhoff M. HybridMT: a MATLAB/shell environment package for seismic moment tensor inversion and refinement. Seismol Res Lett 2016 Jul 1;87(4):964–76. https://doi.org/10.1785/0220150251.
[41] Ren Y, Vavryčuk V, Wu S, Gao Y. Accurate moment tensor inversion of acoustic emissions and its application to Brazilian splitting test. Int J Rock Mech Min Sci 2021 May 1;141:104707. https://doi.org/10.1016/j.ijrmms.2021.104707.
[42] Sellers EJ, Kataka MO, Linzer LM. Source parameters of acoustic emission events and scaling with mining-induced seismicity. J Geophys Res Solid Earth 2003 Sep;108(B9). https://doi.org/10.1029/2001JB000670.
[43] Alamos Gold Inc. Ground control management plan. 2020.